

# Ligand recognition and gating mechanism through three ligand-binding sites of human TRPM2 channel

Yihe Huang, Becca Roth, Wei Lü\*, Juan Du\*

Van Andel Institute, Grand Rapids, United States

**Abstract** TRPM2 is critically involved in diverse physiological processes including core temperature sensing, apoptosis, and immune response. TRPM2's activation by  $\text{Ca}^{2+}$  and ADP ribose (ADPR), an  $\text{NAD}^+$ -metabolite produced under oxidative stress and neurodegenerative conditions, suggests a role in neurological disorders. We provide a central concept between triple-site ligand binding and the channel gating of human TRPM2. We show consecutive structural rearrangements and channel activation of TRPM2 induced by binding of ADPR in two indispensable locations, and the binding of  $\text{Ca}^{2+}$  in the transmembrane domain. The 8-Br-cADPR—an antagonist of cADPR—binds only to the MHR1/2 domain and inhibits TRPM2 by stabilizing the channel in an apo-like conformation. We conclude that MHR1/2 acts as a orthostatic ligand-binding site for TRPM2. The NUDT9-H domain binds to a second ADPR to assist channel activation in vertebrates, but not necessary in invertebrates. Our work provides insights into the gating mechanism of human TRPM2 and its pharmacology.

DOI: <https://doi.org/10.7554/eLife.50175.001>

## Introduction

ADP ribose (ADPR) and its derivatives, which are products of  $\text{NAD}^+$  metabolism, play essential roles in neurotoxicity and cellular signaling under many physiological and pathological conditions (Ernst et al., 2013; Gasser et al., 2006; Guse, 2015; Kolisek et al., 2005; Nikiforov et al., 2015). In neurodegenerative diseases, the progressive accumulation of poly-ADPR and free ADPR results from poly(adenosine 5'-diphosphate-ribose) polymerase-1 activation, and contributes to neurotoxicity and neuronal death (Kam et al., 2018). Intracellular ADPR targets and activates the nonselective, calcium-permeable TRPM2 channel in the presence of  $\text{Ca}^{2+}$ . ADPR acts on one hand as a secondary messenger that contributes to insulin secretion, redox, and temperature sensation, but on the other hand, its accumulation results in intracellular calcium overload and eventually apoptosis (Hara et al., 2002; Hecquet et al., 2014; Song et al., 2016; Tan and McNaughton, 2016; Togashi et al., 2006; Uchida et al., 2011; Wehage et al., 2002). TRPM2 is thus considered to be a key contributor in brain injury via a glutamate-independent pathway in neurodegenerative conditions or after stroke, and it has important functions in obesity, diabetes, bipolar disorder, and Alzheimer's disease (Aminzadeh et al., 2018; Jang et al., 2015; Sita et al., 2018; Uchida and Tominaga, 2014; Zhang et al., 2012).

Belonging to the transient receptor potential melastatin family (TRPM), TRPM2 shares a characteristic MHR1-4 domain, a transmembrane domain (TMD), and a coiled-coil domain with the other family members. It is unique due to owning a characteristic C-terminal NUDT9-H domain, which has been considered a classic binding site for ADPR and its derivatives (Fliegert et al., 2017; Perraud et al., 2001), but the presence of the ADPR binding site has not been directly observed. Recently, our group defined a novel ADPR binding site in the MHR1/2 domain that is essential for the activation of the zebrafish TRPM2 (drTRPM2) channel (Huang et al., 2018). It remains unclear

### \*For correspondence:

wei.lu@vai.org (WLü);  
juan.du@vai.org (JD)

**Competing interests:** The authors declare that no competing interests exist.

**Funding:** See page 13

**Received:** 12 July 2019

**Accepted:** 11 September 2019

**Published:** 12 September 2019

**Reviewing editor:** Leon D Islas, Universidad Nacional Autónoma de México, Mexico

© Copyright Huang et al. This article is distributed under the terms of the [Creative Commons Attribution License](https://creativecommons.org/licenses/by/4.0/), which permits unrestricted use and redistribution provided that the original author and source are credited.

whether the MHR1/2 domain is a universal binding site across all species; whether the NUDT9-H domain has a second ADPR binding site; and what the functional role of the NUDT9-H domain is. Beyond the agonist ADPR, TRPM2 also responds to a variety of ADPR orthologues including the agonist cyclic ADPR (cADPR) (Kolisek et al., 2005; Yu et al., 2019), which is produced during acute kidney injury (Kolisek et al., 2005; Togashi et al., 2006), and the antagonist 8-bromo-cyclic ADP-ribose (8-Br-cADPR), which decreases ischemia-reperfusion injury when used in treatment (Eraslan et al., 2019). Interestingly, 8-Br-cADPR is an antagonist for cADPR but does not inhibit ADPR-evoked currents (Kolisek et al., 2005). Despite extensive studies (Baszczyński et al., 2019; Eraslan et al., 2019; Fliegert et al., 2018; Fourgeaud et al., 2019; Kolisek et al., 2005; Kühn et al., 2019; Moreau et al., 2013; Tóth and Csanády, 2010), there is limited knowledge about the TRPM2 drug binding sites and how drugs manipulate channel function.

Human TRPM2 (*hsTRPM2*) has several functional properties different from those of *drTRPM2* and invertebrate TRPM2, including temperature sensitivity and desensitization rate (Nam Tran et al., 2018; Iordanov et al., 2019). A recent publication suggested that *hsTRPM2* does not bind ADPR in the MHR1/2 domain and that its activation is rather driven by ADPR binding in the NUDT9-H domain (Wang et al., 2018). However, this suggestion was based on a cryo-electron microscopy (cryo-EM) structure of *hsTRPM2* in the presence of ADPR and  $\text{Ca}^{2+}$  at 6.4 Å, a resolution that cannot clarify whether ADPR is present in either the MHR1/2 or the NUDT9-H domain. Moreover, the assignment of the functional states of the structures in this paper is not clear because there is a lack of side-chain densities in the ADPR/ $\text{Ca}^{2+}$ -bound structure and because the transmembrane domain (TMD) in the apo structure is barely visible.

To understand the mechanism underlying agonist and antagonist recognition, and gating mechanism of human TRPM2, we used single-particle cryo-EM to determine four full-length *hsTRPM2* structures: in the apo state in the presence of EDTA (EDTA-*hsTRPM2*); in a non-activated state in complex with the agonist ADPR (ADPR-*hsTRPM2*); in a pre-open or an inactive state in the presence of ADPR/ $\text{Ca}^{2+}$  (ADPR/ $\text{Ca}^{2+}$ -*hsTRPM2*); and in an inhibited state with the cADPR antagonist 8-Br-cADPR in the presence of  $\text{Ca}^{2+}$  (8-Br-cADPR/ $\text{Ca}^{2+}$ -*hsTRPM2*), at 3.3, 4.4, 3.7, and 3.7 Å, respectively (Figure 1—figure supplements 1 and 2).

## Results

### Structure determination of *hsTRPM2*

In our four *hsTRPM2* structures, the densities for nearly the entire intracellular domain are well-defined, including the NUDT9-H domain and the  $\beta$ 1- $\beta$ 2 loop of the MHR1 domain (Figure 1a–d, Figure 1—figure supplement 3), which were poorly defined or unresolved in the *drTRPM2* structures (Huang et al., 2018). In both ADPR-bound structures, ADPR densities were observed in two different sites on each subunit, one (ADPR1) in the cleft of the MHR1/2 domain and a second (ADPR2) in the cleft of the NUDT9-H domain (Figure 1b,c,f,g; Figure 1—figure supplement 4). In contrast, we found a ring-shaped 8-Br-cADPR density only in the cleft of the MHR1/2 domain of the 8-Br-cADPR/ $\text{Ca}^{2+}$ -*hsTRPM2* structure (Figure 1d,h; Figure 1—figure supplement 4). In addition,  $\text{Ca}^{2+}$  density was visible in the ADPR/ $\text{Ca}^{2+}$ - and 8-Br-cADPR/ $\text{Ca}^{2+}$ -*hsTRPM2* maps (Figure 1g,h), in the same location as in the *hsTRPM4*, *Ficedula albicollis* TRPM8 (*faTRPM8*), *drTRPM2*, and *Nematostella vectensis* TRPM2 (*nvTRPM2*) structures (Autzen et al., 2018; Huang et al., 2018; Yin et al., 2019a; Zhang et al., 2018).

While the majority of the TMD is also well-defined in the four *hsTRPM2* structures (Figure 1—figure supplement 3e–h), less well resolved are the extracellular half of the pore-lining helix S6, the pore helix/loop, and the extracellular loops, similar to those in the TRPM8 structures (Yin et al., 2019a; Yin et al., 2018). Nevertheless, we were able to trace the protein backbone in the S6 helix. We speculate that the poorly defined pore region is caused, at least partially, by  $\beta$ -mercaptoethanol, which is essential for stabilizing the protein during purification but may reduce the conserved disulfide bond formed by C996 and C1008 in the extracellular loops that is important for channel function (Jang et al., 2019; Mei et al., 2006; Mittal et al., 2017; Mittal et al., 2015). That bond is a key interaction that stabilizes the integrity of the pore region in the *drTRPM2* structure (Huang et al., 2018).

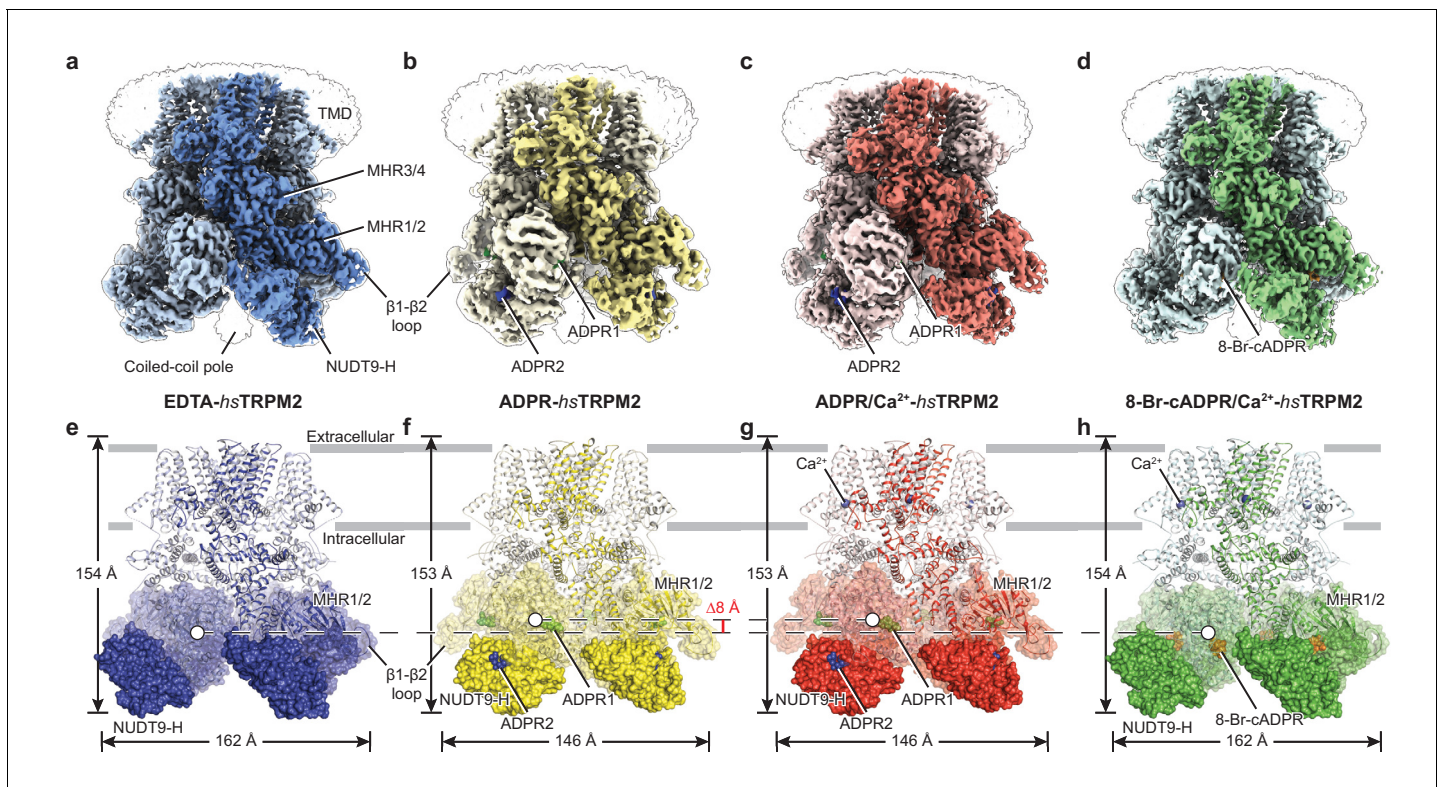


**Figure 1.** The overall architecture of *hsTRPM2*. The three-dimensional reconstructions of (a) EDTA-*hsTRPM2*, (b) ADPR-*hsTRPM2*, (c) ADPR/Ca<sup>2+</sup>-*hsTRPM2*, and (d) 8-Br-cADPR/Ca<sup>2+</sup>-*hsTRPM2*. The unsharpened reconstructions are shown as transparent envelopes. One subunit is highlighted. (e–h) Atomic models of the corresponding reconstructions in panels a–d. The NUDT9-H domains are shown in solid surface, the MHR1/2 domains are shown in transparent surface, and the rest of the proteins are shown in cartoon representation. Ca<sup>2+</sup>, ADPR1, ADPR2, and 8-Br-cADPR are shown in purple, green, blue, and orange spheres, respectively. The center-of-mass (COM) of the MHR1/2 domain of one subunit in each structure is shown as a circle filled with white. The dimensions of the proteins and the difference between COMs along the pore axis are labeled.

DOI: <https://doi.org/10.7554/eLife.50175.002>

The following figure supplements are available for figure 1:

**Figure supplement 1.** The cryo-EM data processing flowchart for *hsTRPM2* using the data of ADPR/Ca<sup>2+</sup>-*hsTRPM2* as an example.

DOI: <https://doi.org/10.7554/eLife.50175.003>

**Figure supplement 2.** Cryo-EM data analysis of *hsTRPM2*.

DOI: <https://doi.org/10.7554/eLife.50175.004>

**Figure supplement 3.** Local resolution estimation and representative densities of *hsTRPM2* structures.

DOI: <https://doi.org/10.7554/eLife.50175.005>

**Figure supplement 4.** Ligand densities.

DOI: <https://doi.org/10.7554/eLife.50175.006>

**Figure supplement 5.** Comparison of the structures of *hsTRPM2*, *drTRPM2*, and *nvTRPM2*.

DOI: <https://doi.org/10.7554/eLife.50175.007>

## Overall architecture and structural comparison

The *hsTRPM2* structures share a four-layer arrangement with *drTRPM2* (Huang et al., 2018; Yin et al., 2019b), having a TMD, MHR3/4, and a ligand-sensing layer that includes the MHR1/2 and NUDT9-H domains, from top to bottom. However, their overall shapes differ, primarily because the NUDT9-H domain is positioned differently. In the EDTA-*hsTRPM2* structure (Figure 1e, Figure 1—figure supplement 5a), the NUDT9-H domain is clamped between cognate and adjacent MHR1/2 domains, forming both intra- and intersubunit interfaces, while only the intrasubunit interface exists in the EDTA-*drTRPM2* structure (Figure 1—figure supplement 5c). As a consequence, the NUDT9-H domain forms a compact structure interacting with the adjacent MHR1/2 domain in *hsTRPM2*, whereas it hangs freely in the *drTRPM2* on the bottom of the protein. Moreover, the NUDT9-H domain is completely invisible in the *nvTRPM2* structure (Figure 1—figure supplement



5e), despite high resolution of the rest of the protein (Zhang et al., 2018). Such an incrementally tighter coupling between the NUDT9-H domain and the rest of the protein, from invertebrate TRPM2 to human TRPM2, is in line with previous reports that the NUDT9-H domain plays an important role in channel gating of *hs*TRPM2 and *dr*TRPM2, but does not affect the channel gating of *nv*TRPM2 (Fliegert et al., 2017; Kühn and Lückhoff, 2004; Wehage et al., 2002; Yu et al., 2017).

Relative to the apo state (Figure 1e), the binding of ADPR to *hs*TRPM2 yielded a markedly elevated MHR1/2 layer and a contracted NUDT9-H layer, with the NUDT9-H domain swinging toward the pore axis (Figure 1f–g). ADPR molecules were identified, with ADPR1 in the MHR1/2 domain and ADPR2 in the NUDT9-H domain (Figure 2a,c–f). Despite a long-existing consensus view that the NUDT9-H domain binds ADPR, this is the first time that the ADPR density has been visualized in this location (Figure 2d). In addition, the clearly defined ADPR1 in the MHR1/2 domain is consistent with the one observed in the *dr*TRPM2 structure (Figure 1—figure supplement 5b,d) (Huang et al., 2018). Given that key residues in the MHR1/2 site are conserved across species (Figure 2—figure supplement 1) and that the invertebrate *nv*TRPM2 responds to ADPR independent of their NUDT9-H domains (Kühn et al., 2016), our data strongly supports the concept that the ligand-binding site in MHR1/2 is conserved throughout all species.

In contrast to ADPR binding, the binding of 8-Br-cADPR did not produce obvious changes in the overall shape of the protein relative to the apo state, in agreement with the view that a competitive antagonist inhibits the protein by stabilizing it in an apo-like state (Figure 1a,d,e,h; Figure 2b,g). Similar mechanism has been observed for human P2 × 3 receptor, in which the competitive antagonists TNP-ATP and A-317491 stabilize the apo/resting state (Mansoor et al., 2016). Surprisingly, in

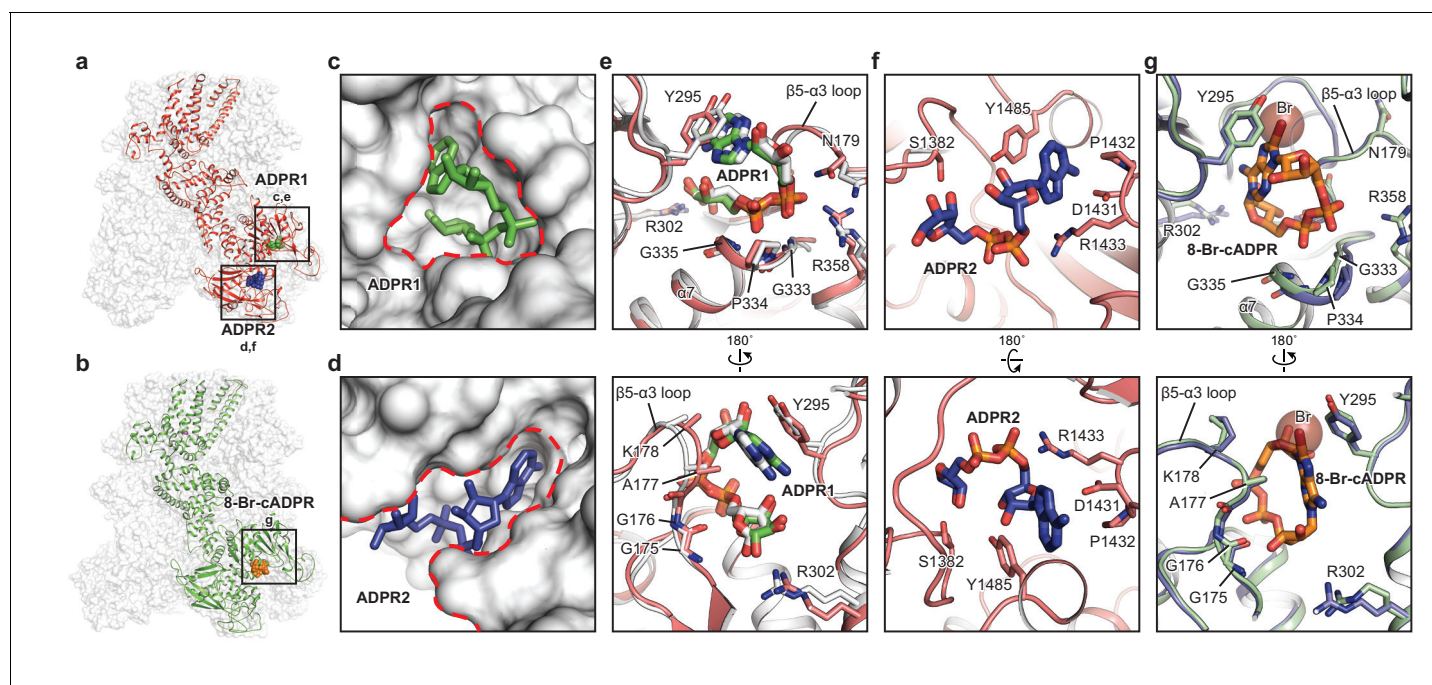


**Figure 2.** The ADPR1, ADPR2, and 8-Br-cADPR binding sites. The structures of the ADPR/Ca<sup>2+</sup>-*hs*TRPM2 (a) and 8-Br-cADPR/Ca<sup>2+</sup>-*hs*TRPM2 (b), with the locations of the ADPR1, ADPR2, and 8-Br-cADPR binding sites boxed. (c–d) Shapes of the ADPR1 (c) and ADPR2 (d) binding sites (outlined by red dashes). ADPR1 and ADPR2 are shown as sticks. (e–g) The ligand binding sites for ADPR1 (e), ADPR2 (f), and 8-Br-cADPR (g). The ligands, and key residues involved in ligand binding are shown as sticks. Superimposition of the human TRPM2 (protein in red and ADPR in green) with the zebrafish TRPM2 (white) shows that the ADPR1 sites are conserved in both organisms (e). Superimposition of the EDTA-*hs*TRPM2 with 8-Br-cADPR/Ca<sup>2+</sup>-*hs*TRPM2 shows that binding of 8-Br-cADPR barely induces conformational change of the ADPR1 binding site. The bromine atom is shown as transparent sphere.

DOI: <https://doi.org/10.7554/eLife.50175.008>

The following figure supplement is available for figure 2:

**Figure supplement 1.** Secondary structure arrangement of *hs*TRPM2 and sequence alignment of TRPM2 from selected species.

DOI: <https://doi.org/10.7554/eLife.50175.009>

our 8-Br-cADPR/Ca<sup>2+</sup>-*hsTRPM2* structure, the 8-Br-cADPR molecule is observed only in the cleft of MHR1/2 domain (**Figure 2b**), but not in the NUDT9-H domain as previously proposed (Eraslan *et al.*, 2019; Kolisek *et al.*, 2005). This observation further supports the idea that the MHR1/2 domain is a key ligand-binding site not only for the agonist ADPR but also for the antagonist 8-Br-cADPR of cADPR.

### Ligand-binding sites

The presence of both ADPR and Ca<sup>2+</sup> initiates a rapid opening of *hsTRPM2*, which permits the flow of cations through the ion-conducting pore (Csanády and Töröcsik, 2009; McHugh *et al.*, 2003; Perraud *et al.*, 2001; Starkus *et al.*, 2007). Contrary to the consensus view that the NUDT9-H domain is the only binding site for ADPR and its derivatives, we found that the MHR1/2 domain binds both ADPR and 8-Br-cADPR, whereas NUDT9-H is only accessible to ADPR. Although both sites bind ADPR, the shapes of the two binding sites are distinct, which means that access is limited to ligands of a certain molecular geometry (**Figure 2a,c,d**).

The binding site in the bi-lobed MHR1/2 cleft is relatively deep, small, and circular. Therefore, ADPR1 is bent into a compact U shape to adapt to the MHR1/2 site (**Figure 2c**), similar to the finding in the *drTRPM2* structure (**Figure 2e**) (Huang *et al.*, 2018). ADPR1 is clamped between Y295 and the loop connecting the  $\beta 5$  strand  $\alpha 3$  helix ( $\beta 5$ - $\alpha 3$  loop), with the terminal adenine and terminal ribose moieties close to each other (**Figure 2e**). Two phosphate groups interact with R358 and the N-terminus of the  $\alpha 7$  helix, while the ribose moiety of the adenosine group coordinates with R302.

In contrast, the cleft in the NUDT9-H domain is wider, embraced by its cap and core regions on each side and the central  $\beta$  sheet on the bottom, allowing ADPR2 to nestle in an extended shape with the terminal adenine and terminal ribose moieties far apart (**Figure 2d**). The adenine moiety of ADPR2 stacks between Y1485 and D1431, while the  $\alpha$ -phosphate group interacts with R1433 (**Figure 2f**). The  $\beta$ -phosphate group and the terminal ribose group are less well defined, presumably due to lack of interaction with the protein. ADPR2 in such an extended shape has been observed in other high-resolution structures such as the human protein ADP-ribosylarginine hydrolase (Rack *et al.*, 2018).

The 8-Br-cADPR shares a similar shape with the U-shaped ADPR1 by connecting the terminal adenine and terminal ribose moieties, but it differs from the extended shape of ADPR2, thus fitting only into the MHR1/2 site (**Figure 2b**). While the residues interacting with 8-Br-cADPR, including Y295 and residues in the  $\beta 5$ - $\alpha 3$  loop, are mostly the same as those interacting with ADPR1, a small displacement of the side chain of Y295 was observed due to the extra bromine atom of 8-Br-cADPR (**Figure 2g**).

To ground of our interpretations of the dual ADPR binding sites in the ligand-sensing domain of TRPM2 in the context of physiological function, we generated mutants of key residues involved in ADPR binding on both sites and we conducted inside-out patch-clamp experiments. Based on several lines of evidence, we concluded that MHR1/2 represents an orthosteric binding site in TRPM2 across all species. First, several mutants of the key residues in the binding site in the MHR1/2 domain either markedly decreased or abolished channel activation in response to ADPR/Ca<sup>2+</sup>, which is caused by either altered affinity of ADPR to the MHR1/2 site, or altered allosteric transition from ligand binding to channel opening, or a combination of both (**Figure 3a–c**). These results indicate that the MHR1/2 binding site is crucial for channel gating of *hsTRPM2*, which agrees with previous functional studies on *hsTRPM2* and *drTRPM2* (Huang *et al.*, 2018; Kashio *et al.*, 2012; Luo *et al.*, 2018). Second, key residues responsible for ligand binding in the MHR1/2 site are highly conserved across species from invertebrates to mammals, whereas those in the NUDT9-H site are less conserved (**Figure 3d**, **Figure 2—figure supplement 1**). Third, ADPR-evoked channel activation of invertebrate *nvTRPM2* is independent of its NUDT9-H domain, because truncation of that domain does not affect channel function (Jordanov *et al.*, 2019; Kühn *et al.*, 2016).

The next question is whether the NUDT9-H site acts as an allosteric binding site or as a second orthosteric binding site. Our electrophysiology data (**Figure 3a**), as well as previous reports by other labs (Fliegert *et al.*, 2017; Yu *et al.*, 2017), showed that mutations of the key residues in the NUDT9-H site markedly affected the channel function of *hsTRPM2*, indicating that this binding site is indispensable for *hsTRPM2* activation. We suggest that the binding of ADPR to the NUDT9-H site assists channel opening in *hsTRPM2*, which will be discussed in the next section.

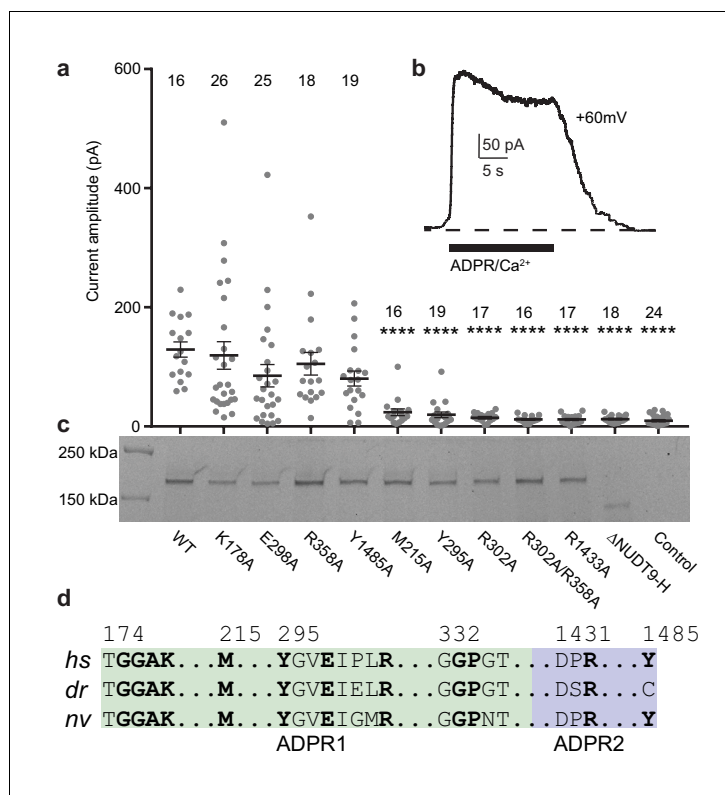


**Figure 3.** Residues and domain that are critical for ADPR-invoked channel activation. (a) Statistics of current amplitudes and cell numbers of inside-out patches pulled from HEK293 cells transfected with wild-type *hsTRPM2*, alanine mutants of key residues in the ADPR1 and ADPR2 sites, and a NUDT9-H-truncated construct,  $\Delta$ NUDT9-H. Control experiments were carried out using non-transfected HEK293 cells. Mutants showing significantly smaller currents than the wild-type *hsTRPM2* are labeled with asterisks (\*\*\*\*;  $p < 0.0001$ ). Data represent the mean  $\pm$  s. e. m. and numbers on the top of each column indicated the number of patches that recorded. Values from individual experiments are shown as filled circles. (b) Representative current in an inside-out patch pulled from HEK293 cell transfected with wild-type *hsTRPM2* cDNA. (c) Surface expression profiles of *hsTRPM2* constructs used in (b), detected by in-gel GFP fluorescence. Most of the mutants showed expression comparable to that of the wild-type *hsTRPM2*; the  $\Delta$ NUDT9-H showed weaker but recognizable expression at lower molecular weight due to truncation of the NUDT9-H domain. (d) Sequence alignment of the ADPR1 and ADPR2 binding sites (*hs* = *Homo sapiens*; *dr* = *Danio rerio*; *nv* = *Nematostella vectensis*). Key residues for ligand binding are in bold.

DOI: <https://doi.org/10.7554/eLife.50175.010>

## Principles of agonist and antagonist actions in channel gating

The coexistence of three ligand-binding sites—a Ca<sup>2+</sup> binding site in the TMD and two ADPR binding sites in the ligand-sensing layer consisting of the MHR1/2 and NUDT9-H domains—endows *hsTRPM2* a complicated gating mechanism. The ADPR- and ADPR/Ca<sup>2+</sup>-*hsTRPM2* structures differ only in the S1-S4 domain, suggesting that the conformational changes induced by Ca<sup>2+</sup> binding is restricted in the TMD and Ca<sup>2+</sup> binding facilitates the channel opening, which agrees with published structures of *drTRPM2* and *hsTRPM4* (Autzen et al., 2018; Huang et al., 2018). Therefore, the intracellular domain is solely manipulated by the ligands binding in the MHR1/2 and NUDT9-H sites.

To understand their relationship with channel gating, we first compared the ligand-sensing layer of the three ligand-bound *hsTRPM2* structures with the apo state structure. Despite a different relative positioning between the NUDT9-H and the MHR1/2 domains, the *hsTRPM2* showed a rearrangement of the ligand-sensing layer upon binding of ADPR similar to that of *drTRPM2* (Figure 4—figure supplement 1a–c) (Huang et al., 2018). These conserved movements include a pendulum swing of the NUDT9-H domain toward pore axis, along with a contraction and clockwise rotation of the entire NUDT9-H layer, and an upward shift and an outward rotation of the MHR1/2 domain. By

contrast, binding of 8-Br-cADPR did not result in an obvious conformational change of these two domains (**Figure 4—figure supplement 1a,d**).

To explore the actions of agonists and antagonists, we compared the MHR1/2 domain and the NUDT9-H domain of *hsTRPM2* in the absence or presence of ligands. ADPR binding into the cleft of MHR1/2 led to a clamshell closure similar to that observed in the *drTRPM2* structures (**Figure 4a**, **Figure 4—figure supplement 1e–f**). Binding of ADPR into the cleft of the NUDT9-H induced a rigid-body rotation of the core region toward the cap region, resulting in a bi-lobed domain closure (**Figure 4b**, **Figure 4—figure supplement 1h–i**). This is the first time that such a motion upon ligand binding has been observed for the NUDT9-H domain, which is likely conserved in its analog – the mitochondrial ADP-ribose pyrophosphatase, NUDT9 (**Shen et al., 2003**).

In contrast, the binding of 8-Br-cADPR barely produced any conformational changes (**Figure 4—figure supplement 1g,j**). Despite the fact that 8-Br-cADPR mimics U-shaped ADPR, the extra bromide atom is obstructed by Y295 (**Figure 2g**), preventing 8-Br-cADPR from going as deep as ADPR into the MHR1/2 cleft. As a result, the phosphate groups of 8-Br-cADPR block helix  $\alpha 7$  from approaching, thus precluding clamshell closure (**Figure 4—figure supplement 1g**). This supports the concept that 8-Br-cADPR acts as an antagonist for cADPR in *hsTRPM2*, which inhibits the channel by occupying and keeping the MHR1/2 clamshell in an open conformation and stabilizing *hsTRPM2* in an apo/resting-like state. Such action of an antagonist has been reported for other ion channels (**Mansoor et al., 2016**).

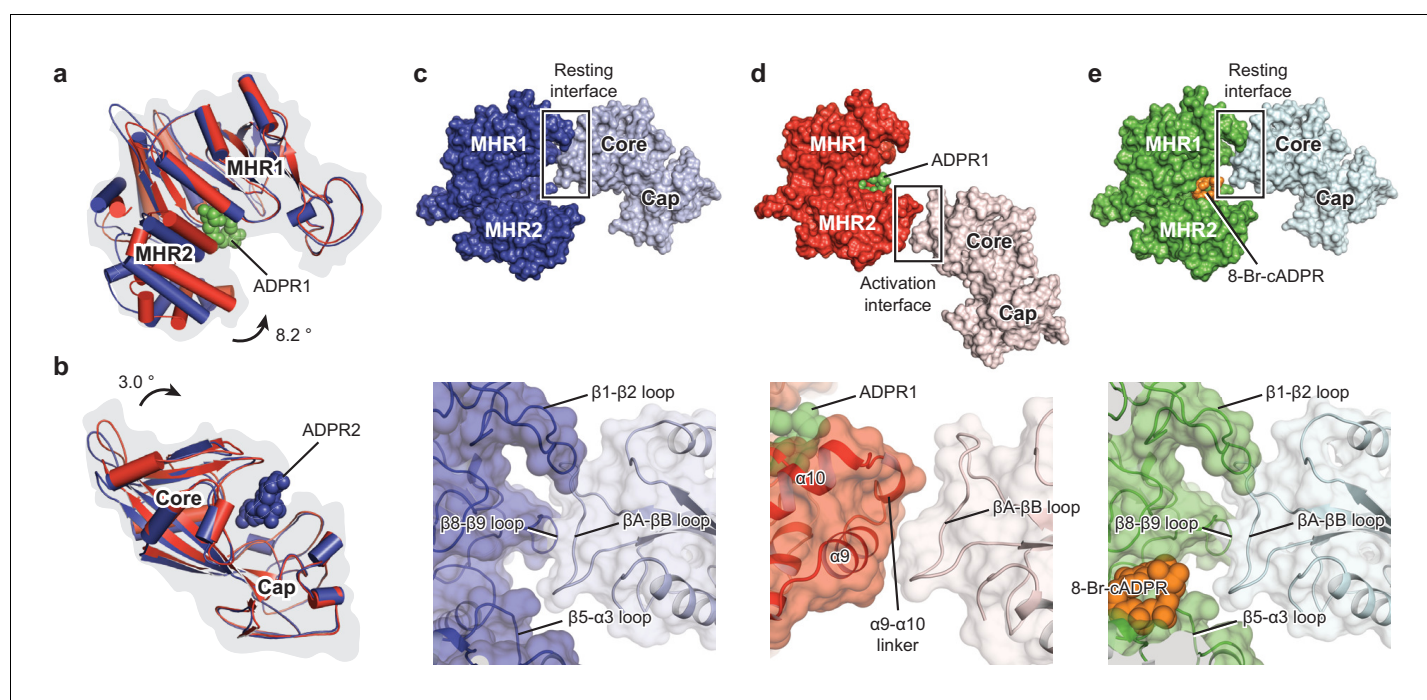


**Figure 4.** Domain rearrangement of the ligand-sensing layer – the MHR1/2 and NUDT9-H domains – upon binding of ADPR or 8-Br-cADPR. Comparison of (a) the MHR1/2 domains and (b) the NUDT9-H domains of EDTA-*hsTRPM2* (blue) and ADPR/Ca<sup>2+</sup>-*hsTRPM2* (red) by superimposition of the MHR1 domains or the cap regions. Domain closure was observed in the MHR1/2 and NUDT9-H domains upon ADPR binding. (c) In the apo resting state, the intersubunit interface (resting interface) is formed by the MHR1 domain and the adjacent core region of the NUDT9-H domain. The rectangle is enlarged in the lower image. (d) Upon binding of ADPR, the intersubunit interface (activation interface) is reorganized and is formed by the MHR2 domain and the adjacent core region. The two adjacent subunits are colored in dark or light colors. Key elements involved in intersubunit interfaces are labeled. (e) Binding of 8-Br-cADPR to the MHR1/2 domain does not result in domain rearrangement of the ligand-sensing layer relative to the apo state shown in panel c.

DOI: <https://doi.org/10.7554/eLife.50175.011>

The following figure supplement is available for figure 4:

**Figure supplement 1.** Conformational rearrangements in the ligand-sensing layer of *hsTRPM2* upon binding of ligands.

DOI: <https://doi.org/10.7554/eLife.50175.012>



On the basis of structural comparison among the *hsTRPM2* structures and the previously published functional studies on invertebrate TRPM2 (Jordanov et al., 2019; Kühn et al., 2016), we suggest that the MHR1/2 clamshell closure is the major driving force of channel opening by initiating motion in the intracellular domain which is transduced to the TMD, eventually causing channel opening in cooperation with  $\text{Ca}^{2+}$ . This raises a key question of why it is necessary to have a second ADPR molecule binding in NUDT9-H for channel activation.

To address this question, we inspected into the ligand-sensing domain upon binding of ADPR and found a striking interface rearrangement between NUDT9-H and the adjacent MHR1/2 domain (Figure 4c–d). In the absence of ADPR, their interface is made of extensive interactions between the core region of NUDT9-H and MHR1 (Figure 4c). Upon binding of ADPR, their interface in the apo resting state is disrupted, and a new interface is created in the activation state between the core region and MHR2 (Figure 4d). Accordingly, we call the interface between MHR1/2 and NUDT9-H a resting interface in the apo state and an activation interface in the ADPR-bound state. Because the core region of the NUDT9-H domain rotates toward the cap region upon binding of ADPR2, we suggest that the ADPR2 may play a role in disrupting the resting interface by pulling the core region away from the adjacent MHR1 domain, which in turn promotes the clamshell closure of MHR1/2 upon binding of ADPR1—a motion that requires flexibility of NUDT9-H that moves along with MHR2, thus assisting channel activation. The binding of 8-Br-cADPR (Figure 4e) did not produce any domain rearrangement relative to the apo state (Figure 4c).

### Channel activation and inhibition

The conformational change of the ligand-sensing layer upon binding of ADPR is transduced to the TMD through MHR3/4, whose motion is conserved between *hsTRPM2* (Figure 5—figure supplement 1) and *drTRPM2* (Huang et al., 2018). To determine the functional states of the four *hsTRPM2* structures, we looked at into their pore regions and compared their TMDs (Figure 5a–g). By comparing the distances between the C $\alpha$  of adjacent pore-restricting residues—N1049 and Q1053—with those in *drTRPM2* (Huang et al., 2018), all four showed an occluded pore, including the ADPR/ $\text{Ca}^{2+}$ -*hsTRPM2* structure (Figure 5c). The EDTA-*hsTRPM2* and the 8-Br-cADPR/ $\text{Ca}^{2+}$ -*hsTRPM2* structures (Figure 5a,d) were nearly identical, and they clearly represented an apo-resting state and an antagonist-bound inhibited closed state, respectively. In contrast, binding of ADPR caused large conformational changes throughout the protein relative to the apo state. Within the TMD specifically, although the pore domain showed little change, the S1-S4 domain underwent a remarkable clockwise rotation around the pore axis (Figure 5e,f). The subtle difference between the S1-S4 domains in ADPR- and ADPR/ $\text{Ca}^{2+}$ -*hsTRPM2* was caused by the binding of  $\text{Ca}^{2+}$  (Figure 5g). The  $\text{Ca}^{2+}$  is coordinated by E843, Q846, N869, D872 and E1073, which are conserved among all the  $\text{Ca}^{2+}$ -sensitive TRPM channels (Figure 5h) (Autzen et al., 2018; Huang et al., 2018; Yamaguchi et al., 2019; Yin et al., 2019a). Because ADPR alone cannot activate the TRPM2 channel in the absence of  $\text{Ca}^{2+}$  (McHugh et al., 2003; Sumoza-Toledo and Penner, 2011), we designated the ADPR-*hsTRPM2* structure as a ADPR-bound non-activated state.

The ADPR/ $\text{Ca}^{2+}$ -*hsTRPM2* structure is closed, unlike the ADPR/ $\text{Ca}^{2+}$ -*drTRPM2* structure, which has a wide, open pore. A key element of the TRPM2 channel opening is the flipping of the S4-S5 linker from one side of the TRP helix to the other as a result of the synergetic actions of ADPR and  $\text{Ca}^{2+}$ , which is derived from our two *drTRPM2* structures (Huang et al., 2018). Indeed, the S4-S5 linkers in the ADPR/ $\text{Ca}^{2+}$ -*hsTRPM2* structure (Figure 5i,j) are un-flipped, indicating that the TMD conformation represents either a pre-open or an inactive state. We favor the former, because the structure of ADPR/ $\text{Ca}^{2+}$ -*hsTRPM2* is nearly identical with the non-activated ADPR-*hsTRPM2*. Moreover, the recently published two-fold symmetric *drTRPM2* adopts a hybrid of alternating non-flipped and flipped conformation of the S4-S5 linkers in TMD (Yin et al., 2019b), the former of which represents an intermediate state after ligand binding but prior to channel opening, which is similar to the TMD conformation of in our ADPR/ $\text{Ca}^{2+}$ -bound *hsTRPM2* structure. This further supports that the ADPR/ $\text{Ca}^{2+}$ -bound *hsTRPM2* structure represents a pre-open state.

We have noted that the published *hsTRPM2* structure in the presence of  $\text{Ca}^{2+}$  and ADPR at 6.4 Å overall resolution was reported as an open state (Wang et al., 2018). However, that interpretation is questionable, not only because most of the transmembrane domain was poorly defined in the cryo-EM map but also because the S4-S5 linker in the ADPR/ $\text{Ca}^{2+}$ -bound structure was clearly on the same side as in the apo resting structure (Wang et al., 2018).



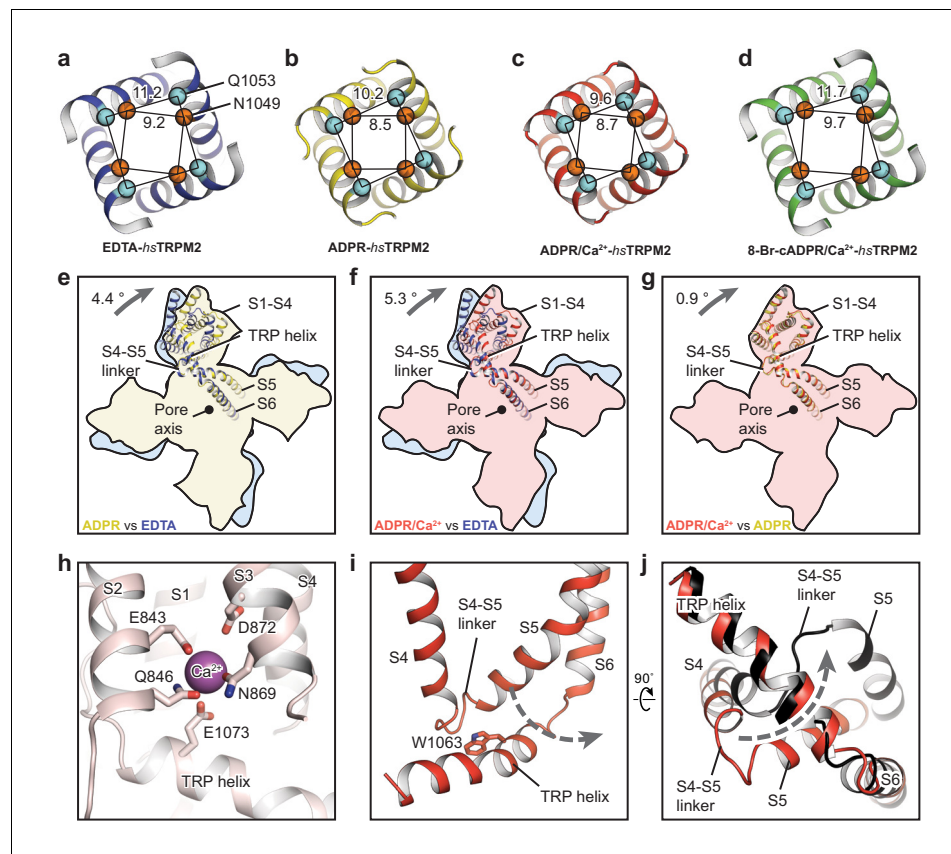


**Figure 5.** The ion-conducting pore. The gates of (a) EDTA-*hsTRPM2*, (b) ADPR-*hsTRPM2*, (c) ADPR/Ca<sup>2+</sup>-*hsTRPM2*, and (d) 8-Br-cADPR/Ca<sup>2+</sup>-*hsTRPM2*, viewed from the intracellular side. The distances between the C $\alpha$  atoms of adjacent N1049 and the distances between the C $\alpha$  atoms of adjacent Q1053 are indicated. (e–g) Comparison of the TMDs of EDTA-*hsTRPM2* and ADPR-*hsTRPM2* (e), EDTA-*hsTRPM2* and ADPR/Ca<sup>2+</sup>-*hsTRPM2* (f), and ADPR-*hsTRPM2* and ADPR/Ca<sup>2+</sup>-*hsTRPM2* (g) by superimposition of their pore domain of the tetramer. While the pore-lining S6 and S5 are well aligned, a clockwise rotation of the S1-S4 domain and TRP helix is observed from EDTA-*hsTRPM2* and ADPR/Ca<sup>2+</sup>-*hsTRPM2*. (h) Calcium binding sites in the ADPR/Ca<sup>2+</sup>-*hsTRPM2* structure. (i) The relative positioning between the S4-S5 linker and the TRP helix in ADPR/Ca<sup>2+</sup>-*hsTRPM2*, viewed parallel to the membrane. The dashed arrow illustrates the proposed movement of the S4-S5 linker from one side to the other of the TRP helix, which is required for channel opening upon binding of ADPR/Ca<sup>2+</sup> that is observed in *drTRPM2* (Huang *et al.*, 2018). (j) Comparison of the S4-S5 linkers in ADPR/Ca<sup>2+</sup>-*hsTRPM2* (red) and ADPR/Ca<sup>2+</sup>-*drTRPM2* (black), viewed from the intracellular side. The two structures are superimposed using the TRP helix.

DOI: <https://doi.org/10.7554/eLife.50175.013>

The following figure supplement is available for figure 5:

**Figure supplement 1.** Conformational changes in the MHR3/4 domains upon binding of ADPR.

DOI: <https://doi.org/10.7554/eLife.50175.014>

## Discussion

A central concept of the relationship between ligand binding and channel gating in TRPM2 arises on the basis of our *hsTRPM2* and *drTRPM2* structures, in which the functional state of the channel correlated with the conformation of the MHR1/2 domain; that is, the channel is in a ligand-free, apo (resting) state or an antagonist-bound inhibited state when MHR1/2 is open, and the channel is in an agonist-bound active state when the MHR1/2 is closed (Figure 6). The channel opening also requires the binding of Ca<sup>2+</sup> in the TMD and a second ADPR molecule in the NUDT9-H domain. Unlike the consensus view of the NUDT9-H domain acting as the primary binding site for ADPR and its analogs, our data suggest that MHR1/2 represents an orthosteric binding site in TRPM2 across species, with key interaction residues conserved from invertebrates to mammals. TRPM2 is one example in which activation of the channel requires the synergetic binding of two ligands in three distinct sites.

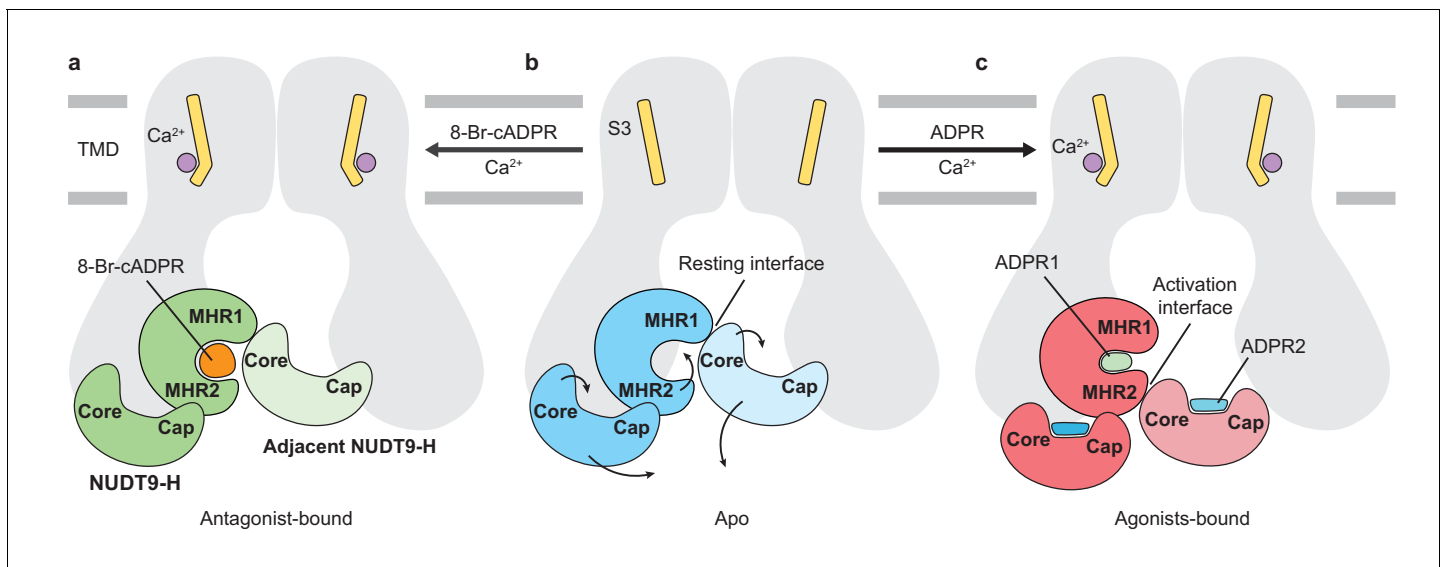


**Figure 6.** Schematic of ligand-sensing of *h*sTRPM2. (a–c) Conformational changes of *h*sTRPM2 among antagonist-bound (a), apo-resting (b), and agonist-bound (c) structures, focusing on the three ligand-binding sites. (a) 8-Br-cADPR binds only to the cleft of the MHR1/2 domain but not to the NUDT9-H domain. It inhibits the channel by stabilizing the MHR1/2 domain in an apo-like conformation. The  $\text{Ca}^{2+}$  binding causes a tilting of the nearby S3 in the TMD, which is suggested to facilitate channel opening in the presence of agonist ADPR (Csanády and Töröcsik, 2009; McHugh et al., 2003; Starkus et al., 2007). However,  $\text{Ca}^{2+}$  alone is not sufficient to open the channel. (c) Conformational changes of *h*sTRPM2 upon binding of  $\text{Ca}^{2+}$  and ADPR in triple binding sites with  $\text{Ca}^{2+}$  bound nearby S3, the U-shaped ADPR1 (green) in the cleft of MHR1/2 domain, and the extended ADPR2 (blue) in the cleft of NUDT9-H domain. Binding of ADPR1 and ADPR2 induces bi-lobed domain closure of the MHR1/2 domain and the NUDT9-H domain, respectively. The MHR1/2 domain shows a counterclockwise rotation and the NUDT9-H domain swings toward the pore center. As a result, the resting interface is disrupted, and an activation interface is created between adjacent subunits. The movements induced by ADPR in the MHR1/2 domain and NUDT9-H domain are shown by arrows.

DOI: <https://doi.org/10.7554/eLife.50175.015>

The following figure supplement is available for figure 6:

**Figure supplement 1.** Comparison of the NUDT9-H domain with the NUDT9 enzyme.

DOI: <https://doi.org/10.7554/eLife.50175.016>

What then is the function of the characteristic NUDT9-H domain? It is indispensable for vertebrate TRPM2 channel activation, including human and zebrafish, but it is not required in invertebrates *nv*TRPM2 (Kühn et al., 2016). Comparison among the available TRPM2 structures reveals different interactions between NUDT9-H and MHR1/2 in human versus invertebrate TRPM2, which seemingly correlates with the functional importance of the NUDT9-H domain. In the *nv*TRPM2, the NUDT9-H domain likely lacks any interface with the rest of the protein, because it is completely invisible in the structure, despite the rest of the protein being well resolved (Zhang et al., 2018). By contrast, the *d*rTRPM2 has a visible but poorly defined NUDT9-H domain with a single major interface between the cognate MHR1/2 and NUDT9-H domains (Huang et al., 2018). Lastly, the *h*sTRPM2 has a well-defined NUDT9-H domain that has two major interfaces with the rest of protein, one with the cognate MHR1/2 and the other with the adjacent MHR1/2 domain. Such an incrementally tighter interaction between the NUDT9-H domain and the rest of protein is in harmony with the fact that the NUDT9-H domain gained more function along the evolution from invertebrates to mammals, such as temperature sensing, redox sensing, and channel gating, to endow TRPM2 with a polymodal nature. In parallel, the NUDT9-H domain has lost the ability to hydrolyze ADPR into AMP and ribose-5-phosphate, a function that exists only in invertebrate TRPM2 and NUDT9 (Iordanov et al., 2016; Iordanov et al., 2019; Tóth et al., 2014). A comparison between NUDT9-H in *h*sTRPM2 and NUDT9 (Shen et al., 2003) shows a wider opening of the cleft in NUDT9 (Figure 6—figure supplement 1), which is likely related to the fact that the core region in *h*sTRPM2 is restricted by the adjacent MHR1/2, whereas NUDT9 lacks such a restriction. Such a restriction for the NUDT9-H domain is

also missing in invertebrate TRPM2 such as *nvTRPM2*, perhaps giving rise to a similar cleft opening as in *NUDT9* and thus preserved enzymatic activity (*Iordanov et al., 2019; Kühn et al., 2016*).

In summary, our human TRPM2 structures defined two distinctive ADPR binding sites, one in the MHR1/2 domain and one in the *NUDT9-H* domain. These structures demonstrate how incorporation of three different ligand binding sites, including the  $\text{Ca}^{2+}$  site in the TMD, regulates channel function. Our work provides a clear structural explanation for ligand recognition, pharmacology, and the gating mechanism of the polymodal TRPM2 channel.

## Materials and methods

### Construct description, Expression and purification of full-length human TRPM2

The full-length human *TRPM2* gene (UniProtKB - O94759) was synthesized by Bio Basic and subcloned into a pEG BacMam vector with a twin-Strep tag, His<sub>6</sub> tag, enhanced green fluorescent protein (eGFP), and a thrombin cleavage site at the N terminus of the gene (*Goehring et al., 2014; Haley et al., 2019*). Plasmid DNA for the *hsTRPM2* construct was transformed into DH5alpha competent cells, expanded into a large-scale bacterial culture, and isolated using EndoFree Plasmid kits (Qiagen). Purified plasmid DNA was mixed with PEI 25K (Polysciences) in a 3:1 ratio of PEI to DNA (w/w) and incubated at room temperature for 30 min. The PEI-DNA mixture was added to a suspension culture of HEK293 cells (ATCC Cat# CRL-11268, tested negative for mycoplasma contamination) at a density of  $2.5\text{--}3.0 \times 10^6/\text{mL}$  for protein expression. After 12–24 hr post-transfection at 37°C, sodium butyrate (10 mM) was added to the suspension and the temperature was adjusted to 30°C to boost the protein expression. Seventy-two hours after transfection, HEK293 cells were harvested and washed with cold TBS buffer (150 mM NaCl, 20 mM Tris HCl, pH 8.0).

Harvested cells were lysed for 1 hr in 10 mM Tris-HCl pH 8.0 buffer containing a protease inhibitor cocktail (1 mM phenylmethylsulfonyl fluoride (PMSF), 2 mM pepstatin, 0.8 μM aprotinin, and 2 μg/ml leupeptin). After 1 hr of incubation, Tris-HCl pH 8.0 and NaCl were added to final concentrations of 20 mM and 150 mM, respectively. Lysed cells were incubated on ice for an additional 20 min. Cell debris and unlysed cells were removed by centrifugation at 2000 x g for 10 min. Ultracentrifugation was used to collect the membranes, using a 45 Ti rotor at 186,000 x g for 1 hr at 4°C (Beckman Coulter). The collected membranes were homogenized using a Dounce homogenizer in TBS buffer containing a protease inhibitor cocktail and 2 mM 2-mercaptoethanol. Solubilization of the membrane was performed by using 10 mM glyco-diosgenin (Anatrace) for 1 hr at 4°C before ultracentrifugation for 30 min at 186,000 x g. The supernatant was transferred out of centrifuge tubes and incubated with Talon resin (Clontech) for 2 hr. Talon resin was washed with six bed volumes of TBS buffer containing 0.2 mM glyco-diosgenin, 10 mM imidazole, and 2 mM 2-mercaptoethanol. The protein was eluted with TBS buffer containing 0.2 mM glyco-diosgenin, 250 mM imidazole, and 2 mM 2-mercaptoethanol. The protein eluate was collected, concentrated, and loaded onto a Superose 6 column (GE Healthcare) using TBS buffer containing 0.2 mM glyco-diosgenin and 5 mM 2-mercaptoethanol. The peak fractions were combined and concentrated to 6.0–7.0 mg/mL using a 100 kDa concentrator (Millipore).

### Electron microscopy sample preparation and data acquisition

Quantifoil holey carbon grids (Au 1.2/1.3 μm size/hole space, 300 mesh) were glow-discharged for 30 s before preparation. Purified and concentrated *hsTRPM2* protein was incubated with either 1 mM EDTA; 1 mM ADPR (Sigma-Aldrich); 1 mM ADPR (Sigma-Aldrich) plus 1 mM  $\text{CaCl}_2$ ; or 1 mM 8-Br-cADPR (Santa Cruz Biotechnology) plus 1 mM  $\text{CaCl}_2$ . After incubation, 2.5 μl of protein sample was added to the carbon face of the grids and blotted for 2 s with a 5 s waiting time. The grids were plunge-frozen into liquid ethane and then cooled by liquid nitrogen using a Vitrobot Mark III held at 18°C and 100% humidity.

Images were obtained using an FEI Titan Krios electron microscope operating at 300 kV with a nominal magnification of 130,000. Images were recorded by a Gatan K2 Summit direct electron detector, which operated in super-resolution counting mode and with a binned pixel size of 1.074 Å. Each image was dose-fractionated to 40 frames, with a total exposure time of 8 s and 0.2 s per frame. The dose rate was  $6.76 \text{ e}^{-\text{Å}^{-2} \text{ s}^{-1}}$  for each image. Images were recorded using an automated

acquisition program (SerialEM) (*Mastrorarde, 2005*). Nominal defocus values varied between  $-1.3$  to  $-1.9$   $\mu\text{m}$ .

## Electron microscopy data processing

Using MotionCor2 (*Zheng et al., 2017*), images were motion-corrected, summed, and  $2 \times 2$  binned in Fourier space. Defocus values were estimated using Gctf (*Zhang, 2016*). Particles were then picked using Gautomatch (<http://www.mrc-lmb.cam.ac.uk/kzhang/Gautomatch/>) and subjected to an initial reference-free 2D classification using RELION (*Scheres, 2012*). Nine representative 2D class averages were selected to use as templates for automated particle-picking for the entire data set using Gautomatch. The auto-picked particles were then visually checked in order to remove false positives. Several rounds of 2D classification were performed to further clean up the selected particles using RELION (*Scheres, 2012*). The initial reconstruction was obtained using cryoSPARC (*Punjani et al., 2017*). The particles were then placed into ten classes using the 3D classification function in RELION (*Scheres, 2012*), with the initial reconstruction low-pass-filtered to 50  $\text{\AA}$  as a reference model. Particles from classes showing high-resolution features were combined and refined with C4 symmetry using RELION (*Scheres, 2012*) (*Figure 1—figure supplement 1*). The final resolutions reported in *Table 1* are based on the gold standard Fourier shell correlation 0.143 criteria. A soft mask (6.4  $\text{\AA}$  extended from the reconstruction with an additional 6.4  $\text{\AA}$  cosine soft edge, low-pass-filtered to 15  $\text{\AA}$ ) was applied to the two half maps in order to calculate the Fourier shell correlation plot. Local resolutions were estimated using Bsoft (*Heymann, 2018*).

**Table 1.** Statistics of 3D reconstruction and model refinement.

Data collection/processing	EDTA- <i>hsTRPM2</i>	ADPR- <i>hsTRPM2</i>	ADPR/ $\text{Ca}^{2+}$ - <i>hsTRPM2</i>	8-Br-cADPR/ $\text{Ca}^{2+}$ - <i>hsTRPM2</i>
Microscope	Titan Krios (FEI)	Titan Krios (FEI)	Titan Krios (FEI)	Titan Krios (FEI)
Voltage (kV)	300	300	300	300
Defocus range ( $\mu\text{M}$ )	1.0–2.5	1.0–2.5	1.0–2.5	1.0–2.5
Exposure time (s)	8	8	8	8
Dose rate ( $\text{e}^-/\text{\AA}^2/\text{s}$ )	6.8	6.8	6.8	6.8
Number of frames	40	40	40	40
Pixel size ( $\text{\AA}$ )	1.076	1.076	1.076	1.076
Particles picked	783,885	537,671	2,342,060	1,822,211
Particles 2D	415,415	346,032	759,700	729,269
Particles refined	161,360	117,350	287,184	102,259
Resolution ( $\text{\AA}$ )	3.3	4.4	3.7	3.7
FSC threshold	0.143	0.143	0.143	0.143
Resolution range ( $\text{\AA}$ )	322.2–3.3	322.2–4.4	322.2–3.7	322.2–3.7
<b>Model statistics</b>				
Number of atoms	37816	37308	37408	38492
Protein	37816	37020	37116	38344
Ligand	0	288	292	148
r.m.s. deviations				
Bond length ( $\text{\AA}$ )	0.007	0.008	0.009	0.006
Bond angle ( $^\circ$ )	0.907	1.015	1.051	0.941
Ramachandran plot				
Favored (%)	92.18	91.59	91.53	94.33
Allowed (%)	7.59	8.02	8.08	5.44
Disallowed (%)	0	0	0	0
Rotamer outlier (%)	0.35	1.40	1.38	1.13

DOI: <https://doi.org/10.7554/eLife.50175.017>



## Model building and structural determination

Models for human TRPM2 were built in Coot using the zebrafish TRPM2 structure as a reference (RCSB Protein Data Bank (PDB) ID: 6DRK and 6DRJ) (Huang *et al.*, 2018). The initial models were then subjected to real space refinement using phenix.real\_space\_refine (Afonine *et al.*, 2012) with secondary-structure restraints. The refined model was further manually examined and adjusted in Coot (Emsley *et al.*, 2010). For validation of the refined structure, Fourier shell correlation curves were applied to calculate the difference between the final model and electron microscopy map by PHENIX comprehensive validation (cryo-EM) (Afonine *et al.*, 2018). The geometries of the atomic models were evaluated using MolProbity (Williams *et al.*, 2018) in PHENIX suite (Adams *et al.*, 2010). All figures were prepared using UCSF Chimera (Pettersen *et al.*, 2004) and ChimeraX (Goddard *et al.*, 2018) and PyMOL (<https://pymol.org>).

## Electrophysiology

HEK293 cells were transfected using Lipofectamine 2000 (Thermo Fisher) according to the manufacturer's protocol. Transfected cells were plated in a 24-well plate and incubated at 37°C. The surface expression of WT human TRPM2 and mutants were evaluated by Pierce cell surface protein isolation kit (Thermo Fisher) according to the manufacturer's protocol, except that the protein was eluted by TBS buffer supplemented with 50 mM Dithiothreitol (DTT) and detected by in-gel fluorescence. Currents from inside-out patches were recorded 12–24 hr post transfection and the recordings were performed by using a HEKA EPC-10 amplifier set to room temperature with a holding potential of +60 mV. The patch pipettes used for these experiments were filled with internal solution that consisted of 150 mM NaCl, 3 mM KCl, and 10 mM HEPES (pH 7.4, adjusted with NaOH). The bath solution was the same as the internal solution. A bath solution with 0.1 mM ADPR and 1 mM CaCl<sub>2</sub> was used to activate the *hs*TRPM2 channel expressed in HEK293 cells. To change the solution, a two-barrel theta-glass pipette controlled manually was used. Data was acquired at 10 kHz using Patchmaster software (HEKA) and for display purposes, data was digitally filtered at 100 Hz and down sampled by a factor of 10. Statistical analysis was done by GraphPad Prism (GraphPad Software), data was reported as mean ± s. e. m. and analyzed using an unpaired *t* - test.

## Data availability

The cryo-EM density map and coordinates of the *hs* TRPM2 apo state, the ADPR-bound state, the ADPR/Ca<sup>2+</sup>-bound state, and the 8-Br-cADPR/Ca<sup>2+</sup>-bound state have been deposited in the Electron Microscopy Data Bank (EMDB) under accession numbers EMD-20478, EMD-20479, EMD-20480 and EMD-20482 and in the Research Collaboratory for Structural Bioinformatics Protein Data Bank under accession codes 6PUO, 6PUR, 6PUS and 6PUU.

## Acknowledgements

We thank G Zhao and X Meng for the support with data collection at the David Van Andel Advanced Cryo-Electron Microscopy Suite. We appreciate the HPC team in VARI for computational support. We thank W Sun (Janelia Research Campus) for his helpful discussion on electrophysiology experiments. We thank D Nadziejka for technical editing. JD is supported by a McKnight Scholar Award, a Klingenstein-Simon Scholar Award and the National Institutes of Health (NIH) (grant 1R01NS111031-01; JD).

---

## Additional information

### Funding

Funder	Grant reference number	Author
Esther A. and Joseph Klingenstein Fund	2019 class	Juan Du
McKnight Endowment Fund for Neuroscience	2019 class	Juan Du
National Institutes of Health	R01NS111031	Juan Du

The funders had no role in study design, data collection and interpretation, or the decision to submit the work for publication.

### Author contributions

Yihe Huang, Data curation, Software, Formal analysis, Validation, Visualization, Methodology, Writing—review and editing; Becca Roth, Data curation, Validation, Methodology, Writing—review and editing; Wei Lü, Conceptualization, Resources, Data curation, Software, Formal analysis, Supervision, Validation, Investigation, Visualization, Methodology, Writing—original draft, Project administration, Writing—review and editing; Juan Du, Conceptualization, Resources, Data curation, Software, Formal analysis, Supervision, Funding acquisition, Validation, Investigation, Visualization, Methodology, Writing—original draft, Project administration, Writing—review and editing

### Author ORCIDs

Wei Lü  <https://orcid.org/0000-0002-3009-1025>

Juan Du  <https://orcid.org/0000-0003-1467-1203>

### Decision letter and Author response

Decision letter <https://doi.org/10.7554/eLife.50175.028>

Author response <https://doi.org/10.7554/eLife.50175.029>

## Additional files

### Supplementary files

- Transparent reporting form

DOI: <https://doi.org/10.7554/eLife.50175.018>

### Data availability

All the cryo-EM data generated in this study have been deposited to PDB and EMDB databank.

The following datasets were generated:

Author(s)	Year	Dataset title	Dataset URL	Database and Identifier
Du J, Lu W, Huang Y	2019	Human TRPM2 in the apo state	<a href="http://www.rcsb.org/structure/6PUO">http://www.rcsb.org/structure/6PUO</a>	Protein Data Bank, 6PUO
Du J, Lu W, Huang Y	2019	Human TRPM2 bound to ADPR and calcium	<a href="http://www.rcsb.org/structure/6PUS">http://www.rcsb.org/structure/6PUS</a>	Protein Data Bank, 6PUS
Du J, Lu W, Huang Y	2019	Human TRPM2 bound to ADPR	<a href="http://www.rcsb.org/structure/6PUR">http://www.rcsb.org/structure/6PUR</a>	Protein Data Bank, 6PUR
Du J, Lu W, Huang Y	2019	Human TRPM2 bound to 8-Br-cADPR and calcium	<a href="http://www.rcsb.org/structure/6PUU">http://www.rcsb.org/structure/6PUU</a>	Protein Data Bank, 6PUU

## References

- Adams PD, Afonine PV, Bunkóczi G, Chen VB, Davis IW, Echols N, Headd JJ, Hung LW, Kapral GJ, Grosse-Kunstleve RW, McCoy AJ, Moriarty NW, Oeffner R, Read RJ, Richardson DC, Richardson JS, Terwilliger TC, Zwart PH. 2010. *PHENIX*: a comprehensive Python-based system for macromolecular structure solution. *Acta Crystallographica Section D Biological Crystallography* **66**:213–221. DOI: <https://doi.org/10.1107/S0907444909052925>, PMID: 20124702
- Afonine PV, Grosse-Kunstleve RW, Echols N, Headd JJ, Moriarty NW, Mustyakimov M, Terwilliger TC, Urzhumtsev A, Zwart PH, Adams PD. 2012. Towards automated crystallographic structure refinement with *phenix.refine*. *Acta Crystallographica Section D Biological Crystallography* **68**:352–367. DOI: <https://doi.org/10.1107/S0907444912001308>, PMID: 22505256
- Afonine PV, Klaholz BP, Moriarty NW, Poon BK, Sobolev OV, Terwilliger TC, Adams PD, Urzhumtsev A. 2018. New tools for the analysis and validation of cryo-EM maps and atomic models. *Acta Crystallographica Section D Structural Biology* **74**:814–840. DOI: <https://doi.org/10.1107/S2059798318009324>
- Aminzadeh M, Roghani M, Sarfallah A, Riaz GH. 2018. TRPM2 dependence of ROS-induced NLRP3 activation in Alzheimer's disease. *International Immunopharmacology* **54**:78–85. DOI: <https://doi.org/10.1016/j.intimp.2017.10.024>, PMID: 29107864

- Autzen HE**, Myasnikov AG, Campbell MG, Asarnow D, Julius D, Cheng Y. 2018. Structure of the human TRPM4 ion channel in a lipid nanodisc. *Science* **359**:228–232. DOI: <https://doi.org/10.1126/science.aar4510>
- Baszczyński O**, Watt JM, Rozewitz MD, Guse AH, Fliegert R, Potter BVL. 2019. Synthesis of terminal ribose analogues of adenosine 5'-Diphosphate ribose as probes for the transient receptor potential cation channel TRPM2. *The Journal of Organic Chemistry* **84**:6143–6157. DOI: <https://doi.org/10.1021/acs.joc.9b00338>, PMID: 30978018
- Csanády L**, Töröcsik B. 2009. Four Ca<sup>2+</sup> ions activate TRPM2 channels by binding in deep crevices near the pore but intracellularly of the gate. *The Journal of General Physiology* **133**:189–203. DOI: <https://doi.org/10.1085/jgp.200810109>, PMID: 19171771
- Drozdetskiy A**, Cole C, Procter J, Barton GJ. 2015. JPred4: a protein secondary structure prediction server. *Nucleic Acids Research* **43**:W389–W394. DOI: <https://doi.org/10.1093/nar/gkv332>, PMID: 25883141
- Emsley P**, Lohkamp B, Scott WG, Cowtan K. 2010. Features and development of coot. *Acta Crystallographica. Section D, Biological Crystallography* **66**:486–501. DOI: <https://doi.org/10.1107/S0907444910007493>, PMID: 20383002
- Eraslan E**, Tanyeli A, Polat E, Polat E. 2019. 8-Br-cADPR, a TRPM2 ion channel antagonist, inhibits renal ischemia-reperfusion injury. *Journal of Cellular Physiology* **234**:4572–4581. DOI: <https://doi.org/10.1002/jcp.27236>, PMID: 30191993
- Ernst IM**, Fliegert R, Guse AH. 2013. Adenine dinucleotide second messengers and T-lymphocyte calcium signaling. *Frontiers in Immunology* **4**:259. DOI: <https://doi.org/10.3389/fimmu.2013.00259>, PMID: 24009611
- Fliegert R**, Watt JM, Schöbel A, Rozewitz MD, Moreau C, Kirchberger T, Thomas MP, Sick W, Araujo AC, Harneit A, Potter BVL, Guse AH. 2017. Ligand-induced activation of human TRPM2 requires the terminal ribose of ADPR and involves Arg1433 and Tyr1349. *Biochemical Journal* **474**:2159–2175. DOI: <https://doi.org/10.1042/BCJ20170091>, PMID: 28515263
- Fliegert R**, Hölzer HT, Guse AH. 2018. TRPM2 activation: paradigm shifted? *Cell Calcium* **76**:132–134. DOI: <https://doi.org/10.1016/j.ceca.2018.11.001>, PMID: 30420160
- Fourgeaud L**, Dvorak C, Faouzi M, Starkus J, Sahdeo S, Wang Q, Lord B, Coate H, Taylor N, He Y, Qin N, Wickenden A, Carruthers N, Lovenberg TW, Penner R, Bhattacharya A. 2019. Pharmacology of JNJ-28583113: a novel TRPM2 antagonist. *European Journal of Pharmacology* **853**:299–307. DOI: <https://doi.org/10.1016/j.ejphar.2019.03.043>, PMID: 30965058
- Gasser A**, Glassmeier G, Fliegert R, Langhorst MF, Meinke S, Hein D, Krüger S, Weber K, Heiner I, Oppenheimer N, Schwarz JR, Guse AH. 2006. Activation of T cell calcium influx by the second messenger ADP-ribose. *Journal of Biological Chemistry* **281**:2489–2496. DOI: <https://doi.org/10.1074/jbc.M506525200>, PMID: 16316998
- Goddard TD**, Huang CC, Meng EC, Pettersen EF, Couch GS, Morris JH, Ferrin TE. 2018. UCSF ChimeraX: meeting modern challenges in visualization and analysis. *Protein Science* **27**:14–25. DOI: <https://doi.org/10.1002/pro.3235>, PMID: 28710774
- Goehring A**, Lee CH, Wang KH, Michel JC, Claxton DP, Bacongus I, Althoff T, Fischer S, Garcia KC, Gouaux E. 2014. Screening and large-scale expression of membrane proteins in mammalian cells for structural studies. *Nature Protocols* **9**:2574–2585. DOI: <https://doi.org/10.1038/nprot.2014.173>, PMID: 25299155
- Guse AH**. 2015. Calcium mobilizing second messengers derived from NAD. *Biochimica Et Biophysica Acta (BBA) - Proteins and Proteomics* **1854**:1132–1137. DOI: <https://doi.org/10.1016/j.bbapap.2014.12.015>
- Haley E**, Choi W, Fan C, Sun W, Du J, Lu W. 2019. Expression and purification of the human Lipid-sensitive cation channel TRPC3 for structural determination by Single-particle Cryo-electron microscopy. *Journal of Visualized Experiments*. DOI: <https://doi.org/10.3791/58754>, PMID: 30663716
- Hara Y**, Wakamori M, Ishii M, Maeno E, Nishida M, Yoshida T, Yamada H, Shimizu S, Mori E, Kudoh J, Shimizu N, Kurose H, Okada Y, Imoto K, Mori Y. 2002. LTRPC2 Ca<sup>2+</sup>-permeable channel activated by changes in redox status confers susceptibility to cell death. *Molecular Cell* **9**:163–173. DOI: [https://doi.org/10.1016/S1097-2765\(01\)00438-5](https://doi.org/10.1016/S1097-2765(01)00438-5), PMID: 11804595
- Hecquet CM**, Zhang M, Mittal M, Vogel SM, Di A, Gao X, Bonini MG, Malik AB. 2014. Cooperative interaction of *trp* melastatin channel transient receptor potential (TRPM2) with its splice variant TRPM2 short variant is essential for endothelial cell apoptosis. *Circulation Research* **114**:469–479. DOI: <https://doi.org/10.1161/CIRCRESAHA.114.302414>, PMID: 24337049
- Heymann JB**. 2018. Guidelines for using bsoft for high resolution reconstruction and validation of biomolecular structures from electron micrographs. *Protein Science* **27**:159–171. DOI: <https://doi.org/10.1002/pro.3293>, PMID: 28891250
- Huang Y**, Winkler PA, Sun W, Lu W, Du J. 2018. Architecture of the TRPM2 channel and its activation mechanism by ADP-ribose and calcium. *Nature* **562**:145–149. DOI: <https://doi.org/10.1038/s41586-018-0558-4>, PMID: 30250252
- Iordanov I**, Mihályi C, Tóth B, Csanády L. 2016. The proposed channel-enzyme transient receptor potential melastatin 2 does not possess ADP ribose hydrolase activity. *eLife* **5**:e17600. DOI: <https://doi.org/10.7554/eLife.17600>, PMID: 27383051
- Iordanov I**, Tóth B, Szollosi A, Csanády L. 2019. Enzyme activity and selectivity filter stability of ancient TRPM2 channels were simultaneously lost in early vertebrates. *eLife* **8**:e44556. DOI: <https://doi.org/10.7554/eLife.44556>, PMID: 30938679
- Jang Y**, Lee SH, Lee B, Jung S, Khalid A, Uchida K, Tominaga M, Jeon D, Oh U. 2015. TRPM2, a susceptibility gene for bipolar disorder, regulates glycogen synthase Kinase-3 activity in the brain. *Journal of Neuroscience* **35**:11811–11823. DOI: <https://doi.org/10.1523/JNEUROSCI.5251-14.2015>, PMID: 26311765

- Jang Y**, Lee B, Kim H, Jung S, Lee SH, Lee SY, Jeon JH, Kim IB, Lee SH, Kim BJ, Kim UH, Lee Y, Kim SM, Jeon D, Oh U. 2019. Trpm2 ablation accelerates protein aggregation by impaired ADPR and autophagic clearance in the brain. *Molecular Neurobiology* **56**:3819–3832. DOI: <https://doi.org/10.1007/s12035-018-1309-0>, PMID: 30215158
- Kam TI**, Mao X, Park H, Chou SC, Karuppagounder SS, Umanah GE, Yun SP, Brahmachari S, Panicker N, Chen R, Andrabi SA, Qi C, Poirier GG, Pletnikova O, Troncoso JC, Bekris LM, Leverenz JB, Pantelyat A, Ko HS, Rosenthal LS, et al. 2018. Poly(ADP-ribose) drives pathologic  $\alpha$ -synuclein neurodegeneration in Parkinson's disease. *Science* **362**:eaat8407. DOI: <https://doi.org/10.1126/science.aat8407>, PMID: 30385548
- Kashio M**, Sokabe T, Shintaku K, Uematsu T, Fukuta N, Kobayashi N, Mori Y, Tominaga M. 2012. Redox signal-mediated sensitization of transient receptor potential melastatin 2 (TRPM2) to temperature affects macrophage functions. *PNAS* **109**:6745–6750. DOI: <https://doi.org/10.1073/pnas.1114193109>, PMID: 22493272
- Kolisek M**, Beck A, Fleig A, Penner R. 2005. Cyclic ADP-ribose and hydrogen peroxide synergize with ADP-ribose in the activation of TRPM2 channels. *Molecular Cell* **18**:61–69. DOI: <https://doi.org/10.1016/j.molcel.2005.02.033>, PMID: 15808509
- Kühn FJ**, Kühn C, Winking M, Hoffmann DC, Lückhoff A. 2016. ADP-Ribose activates the TRPM2 channel from the sea Anemone *nematostella vectensis* independently of the NUDT9H domain. *PLOS ONE* **11**:e0158060. DOI: <https://doi.org/10.1371/journal.pone.0158060>, PMID: 27333281
- Kühn FJP**, Watt JM, Potter BVL, Lückhoff A. 2019. Different substrate specificities of the two ADPR binding sites in TRPM2 channels of *Nematostella vectensis* and the role of IDPR. *Scientific Reports* **9**:4985. DOI: <https://doi.org/10.1038/s41598-019-41531-4>, PMID: 30899048
- Kühn FJ**, Lückhoff A. 2004. Sites of the NUDT9-H domain critical for ADP-ribose activation of the cation channel TRPM2. *Journal of Biological Chemistry* **279**:46431–46437. DOI: <https://doi.org/10.1074/jbc.M407263200>, PMID: 15347676
- Luo Y**, Yu X, Ma C, Luo J, Yang W. 2018. Identification of a novel EF-Loop in the N-terminus of TRPM2 channel involved in calcium sensitivity. *Frontiers in Pharmacology* **9**:581. DOI: <https://doi.org/10.3389/fphar.2018.00581>, PMID: 29915540
- Mansoor SE**, Lu W, Oosterheert W, Shekhar M, Tajkhorshid E, Gouaux E. 2016. X-ray structures define human P2X3 receptor gating cycle and antagonist action. *Nature* **538**:66–71. DOI: <https://doi.org/10.1038/nature19367>
- Mastronarde DN**. 2005. Automated electron microscope tomography using robust prediction of specimen movements. *Journal of Structural Biology* **152**:36–51. DOI: <https://doi.org/10.1016/j.jsb.2005.07.007>, PMID: 16182563
- McHugh D**, Flemming R, Xu S-Z, Perraud A-L, Beech DJ. 2003. Critical Intracellular Ca<sup>2+</sup> Dependence of Transient Receptor Potential Melastatin 2 (TRPM2) Cation Channel Activation. *Journal of Biological Chemistry* **278**:11002–11006. DOI: <https://doi.org/10.1074/jbc.M210810200>
- Mei ZZ**, Mao HJ, Jiang LH. 2006. Conserved cysteine residues in the pore region are obligatory for human TRPM2 channel function. *American Journal of Physiology-Cell Physiology* **291**:C1022–C1028. DOI: <https://doi.org/10.1152/ajpcell.00606.2005>, PMID: 16822940
- Mittal M**, Urao N, Hecquet CM, Zhang M, Sudhakar V, Gao XP, Komarova Y, Ushio-Fukai M, Malik AB. 2015. Novel role of reactive oxygen species-activated *trp* melastatin channel-2 in mediating angiogenesis and postischemic neovascularization. *Arteriosclerosis, Thrombosis, and Vascular Biology* **35**:877–887. DOI: <https://doi.org/10.1161/ATVBAHA.114.304802>, PMID: 25675998
- Mittal M**, Nepal S, Tsukasaki Y, Hecquet CM, Soni D, Rehman J, Tirupathi C, Malik AB. 2017. Neutrophil activation of endothelial Cell-Expressed TRPM2 mediates transendothelial neutrophil migration and vascular injury. *Circulation Research* **121**:1081–1091. DOI: <https://doi.org/10.1161/CIRCRESAHA.117.311747>, PMID: 28790198
- Moreau C**, Kirchberger T, Swarbrick JM, Bartlett SJ, Flieger R, Yorgan T, Bauche A, Harneit A, Guse AH, Potter BV. 2013. Structure-activity relationship of adenosine 5'-diphosphoribose at the transient receptor potential melastatin 2 (TRPM2) channel: rational design of antagonists. *Journal of Medicinal Chemistry* **56**:10079–10102. DOI: <https://doi.org/10.1021/jm401497a>, PMID: 24304219
- Nam Tran H**, Hederih J, Numata T, Mori MX, Maegawa S, Hosokawa H, Mori Y. 2018. Functional characterization of zebrafish transient receptor potential melastatin 2. *Biophysical Journal* **114**:641a–642a. DOI: <https://doi.org/10.1016/j.bpj.2017.11.3463>
- Nikiforov A**, Kulikova V, Ziegler M. 2015. The human NAD metabolome: functions, metabolism and compartmentalization. *Critical Reviews in Biochemistry and Molecular Biology* **50**:284–297. DOI: <https://doi.org/10.3109/10409238.2015.1028612>, PMID: 25837229
- Perraud A-L**, Fleig A, Dunn CA, Bagley LA, Launay P, Schmitz C, Stokes AJ, Zhu Q, Bessman MJ, Penner R, Kinet J-P, Scharenberg AM. 2001. ADP-ribose gating of the calcium-permeable LTRPC2 channel revealed by nudix motif homology. *Nature* **411**:595–599. DOI: <https://doi.org/10.1038/35079100>
- Petterson EF**, Goddard TD, Huang CC, Couch GS, Greenblatt DM, Meng EC, Ferrin TE. 2004. UCSF chimera—a visualization system for exploratory research and analysis. *Journal of Computational Chemistry* **25**:1605–1612. DOI: <https://doi.org/10.1002/jcc.20084>, PMID: 15264254
- Punjani A**, Rubinstein JL, Fleet DJ, Brubaker MA. 2017. cryoSPARC: algorithms for rapid unsupervised cryo-EM structure determination. *Nature Methods* **14**:290–296. DOI: <https://doi.org/10.1038/nmeth.4169>
- Rack JGM**, Ariza A, Drown BS, Henfrey C, Bartlett E, Shirai T, Hergenrother PJ, Ahel I. 2018. (ADP-ribose) hydrolases: structural basis for differential substrate recognition and inhibition. *Cell Chemical Biology* **25**:1533–1546. DOI: <https://doi.org/10.1016/j.chembiol.2018.11.001>, PMID: 30472116



- Scheres SH.** 2012. RELION: implementation of a bayesian approach to cryo-EM structure determination. *Journal of Structural Biology* **180**:519–530. DOI: <https://doi.org/10.1016/j.jsb.2012.09.006>, PMID: 23000701
- Shen BW, Perraud AL, Scharenberg A, Stoddard BL.** 2003. The crystal structure and mutational analysis of human NUDT9. *Journal of Molecular Biology* **332**:385–398. DOI: [https://doi.org/10.1016/S0022-2836\(03\)00954-9](https://doi.org/10.1016/S0022-2836(03)00954-9), PMID: 12948489
- Sievers F, Wilm A, Dineen D, Gibson TJ, Karplus K, Li W, Lopez R, McWilliam H, Remmert M, Söding J, Thompson JD, Higgins DG.** 2011. Fast, scalable generation of high-quality protein multiple sequence alignments using clustal omega. *Molecular Systems Biology* **7**:539. DOI: <https://doi.org/10.1038/msb.2011.75>, PMID: 21988835
- Sita G, Hrelia P, Graziosi A, Ravegnini G, Morroni F.** 2018. TRPM2 in the brain: role in health and disease. *Cells* **7**:82. DOI: <https://doi.org/10.3390/cells7070082>
- Song K, Wang H, Kamm GB, Pohle J, Reis FC, Heppenstall P, Wende H, Siemens J.** 2016. The TRPM2 channel is a hypothalamic heat sensor that limits fever and can drive hypothermia. *Science* **353**:1393–1398. DOI: <https://doi.org/10.1126/science.aaf7537>, PMID: 27562954
- Starkus J, Beck A, Fleig A, Penner R.** 2007. Regulation of TRPM2 by extra- and intracellular calcium. *The Journal of General Physiology* **130**:427–440. DOI: <https://doi.org/10.1085/jgp.200709836>, PMID: 17893195
- Sumoza-Toledo A, Penner R.** 2011. TRPM2: a multifunctional ion channel for calcium signalling. *The Journal of Physiology* **589**:1515–1525. DOI: <https://doi.org/10.1113/jphysiol.2010.201855>, PMID: 21135052
- Tan CH, McNaughton PA.** 2016. The TRPM2 ion channel is required for sensitivity to warmth. *Nature* **536**:460–463. DOI: <https://doi.org/10.1038/nature19074>, PMID: 27533035
- Togashi K, Hara Y, Tominaga T, Higashi T, Konishi Y, Mori Y, Tominaga M.** 2006. TRPM2 activation by cyclic ADP-ribose at body temperature is involved in insulin secretion. *The EMBO Journal* **25**:1804–1815. DOI: <https://doi.org/10.1038/sj.emboj.7601083>
- Tóth B, Iordanov I, Csanády L.** 2014. Putative chanzyme activity of TRPM2 cation channel is unrelated to pore gating. *PNAS* **111**:16949–16954. DOI: <https://doi.org/10.1073/pnas.1412449111>, PMID: 25385633
- Tóth B, Csanády L.** 2010. Identification of direct and indirect effectors of the transient receptor potential melastatin 2 (TRPM2) cation channel. *Journal of Biological Chemistry* **285**:30091–30102. DOI: <https://doi.org/10.1074/jbc.M109.066464>, PMID: 20650899
- Uchida K, Dezaki K, Damdindorj B, Inada H, Shiuchi T, Mori Y, Yada T, Minokoshi Y, Tominaga M.** 2011. Lack of TRPM2 impaired insulin secretion and glucose metabolisms in mice. *Diabetes* **60**:119–126. DOI: <https://doi.org/10.2337/db10-0276>, PMID: 20921208
- Uchida K, Tominaga M.** 2014. The role of TRPM2 in pancreatic  $\beta$ -cells and the development of diabetes. *Cell Calcium* **56**:332–339. DOI: <https://doi.org/10.1016/j.ceca.2014.07.001>, PMID: 25084624
- Wang L, Fu TM, Zhou Y, Xia S, Greka A, Wu H.** 2018. Structures and gating mechanism of human TRPM2. *Science* **362**:eaav4809. DOI: <https://doi.org/10.1126/science.aav4809>, PMID: 30467180
- Wehage E, Einfeld J, Heiner I, Jüngling E, Zitt C, Lückhoff A.** 2002. Activation of the cation channel long transient receptor potential channel 2 (LTRPC2) by hydrogen peroxide. A splice variant reveals a mode of activation independent of ADP-ribose. *The Journal of Biological Chemistry* **277**:23150–23156. DOI: <https://doi.org/10.1074/jbc.M112096200>, PMID: 11960981
- Williams CJ, Headd JJ, Moriarty NW, Prisant MG, Videau LL, Deis LN, Verma V, Keedy DA, Hintze BJ, Chen VB, Jain S, Lewis SM, Arendall WB, Snoeyink J, Adams PD, Lovell SC, Richardson JS, Richardson DC.** 2018. MolProbity: more and better reference data for improved all-atom structure validation. *Protein Science* **27**:293–315. DOI: <https://doi.org/10.1002/pro.3330>, PMID: 29067766
- Yamaguchi S, Tanimoto A, Iwasa S, Otsuguro K-ichi.** 2019. TRPM4 and TRPM5 channels share crucial amino acid residues for Ca<sup>2+</sup> sensitivity but not significance of PI(4,5)P<sub>2</sub>. *International Journal of Molecular Sciences* **20**:2012. DOI: <https://doi.org/10.3390/ijms20082012>
- Yin Y, Wu M, Zubcevic L, Borschel WF, Lander GC, Lee SY.** 2018. Structure of the cold- and menthol-sensing ion channel TRPM8. *Science* **359**:237–241. DOI: <https://doi.org/10.1126/science.aan4325>, PMID: 29217583
- Yin Y, Le SC, Hsu AL, Borgnia MJ, Yang H, Lee SY.** 2019a. Structural basis of cooling agent and lipid sensing by the cold-activated TRPM8 channel. *Science* **363**:eaav9334. DOI: <https://doi.org/10.1126/science.aav9334>, PMID: 30733385
- Yin Y, Wu M, Hsu AL, Borschel WF, Borgnia MJ, Lander GC, Lee S-Y.** 2019b. Visualizing structural transitions of ligand-dependent gating of the TRPM2 channel. *bioRxiv*. DOI: <https://doi.org/10.1101/516468>
- Yu P, Xue X, Zhang J, Hu X, Wu Y, Jiang LH, Jin H, Luo J, Zhang L, Liu Z, Yang W.** 2017. Identification of the ADPR binding pocket in the NUDT9 homology domain of TRPM2. *The Journal of General Physiology* **149**:219–235. DOI: <https://doi.org/10.1085/jgp.201611675>, PMID: 28108595
- Yu P, Liu Z, Yu X, Ye P, Liu H, Xue X, Yang L, Li Z, Wu Y, Fang C, Zhao YJ, Yang F, Luo JH, Jiang LH, Zhang L, Zhang L, Yang W.** 2019. Direct gating of the TRPM2 channel by cADPR via specific interactions with the ADPR binding pocket. *Cell Reports* **27**:3684–3695. DOI: <https://doi.org/10.1016/j.celrep.2019.05.067>, PMID: 31216484
- Zhang Z, Zhang W, Jung DY, Ko HJ, Lee Y, Friedline RH, Lee E, Jun J, Ma Z, Kim F, Tsitsilianos N, Chapman K, Morrison A, Cooper MP, Miller BA, Kim JK.** 2012. TRPM2 Ca<sup>2+</sup> channel regulates energy balance and glucose metabolism. *American Journal of Physiology. Endocrinology and Metabolism* **302**:E807–E816. DOI: <https://doi.org/10.1152/ajpendo.00239.2011>, PMID: 22275755
- Zhang K.** 2016. Gctf: real-time CTF determination and correction. *Journal of Structural Biology* **193**:1–12. DOI: <https://doi.org/10.1016/j.jsb.2015.11.003>, PMID: 26592709

- Zhang Z**, Tóth B, Szollosi A, Chen J, Csanády L. 2018. Structure of a TRPM2 channel in complex with  $\text{Ca}^{2+}$  explains unique gating regulation. *eLife* **7**:e36409. DOI: <https://doi.org/10.7554/eLife.36409>, PMID: 29745897
- Zheng SQ**, Palovcak E, Armache JP, Verba KA, Cheng Y, Agard DA. 2017. MotionCor2: anisotropic correction of beam-induced motion for improved cryo-electron microscopy. *Nature Methods* **14**:331–332. DOI: <https://doi.org/10.1038/nmeth.4193>, PMID: 28250466